# Amplitude Distribution of Calcium Sparks in Confocal Images: Theory and Studies with an Automatic Detection Method

Heping Cheng,* Long-Sheng Song,* Natalia Shirokova,# Adom González,# Edward G. Lakatta,* Eduardo Ríos,# and Michael D. Stern*

*Laboratory of Cardiovascular Science, Gerontology Research Center, National Institute on Aging, National Institutes of Health, Baltimore, Maryland 21224; and #Department of Molecular Biophysics and Physiology, Rush University, Chicago, Illinois 60612 USA

ABSTRACT Determination of the calcium spark amplitude distribution is of critical importance for understanding the nature of elementary calcium release events in striated muscle. In the present study we show, on general theoretical grounds, that calcium sparks, as observed in confocal line scan images, should have a nonmodal, monotonic decreasing amplitude distribution, regardless of whether the underlying events are stereotyped. To test this prediction we developed, implemented, and verified an automated computer algorithm for objective detection and measurement of calcium sparks in raw image data. When the sensitivity and reliability of the algorithm were set appropriately, we observed highly left-skewed or monotonic decreasing amplitude distributions in skeletal muscle cells and cardiomyocytes, confirming the theoretical predictions. The previously reported modal or Gaussian distributions of sparks detected by eye must therefore be the result of subjective detection bias against small amplitude events. In addition, we discuss possible situations when a modal distribution might be observed.

## INTRODUCTION

Excitation-contraction coupling in striated muscle takes place by the release of stored calcium from the sarcoplasmic reticulum in response to depolarization of the sarcolemma, via calcium release channels, commonly referred to as ryanodine receptors. In cardiac muscle it is clear that this release is triggered by calcium-induced calcium release (CICR) (Fabiato, 1985), while in skeletal muscle it is believed that an allosteric signal is transmitted to the release channels from sarcolemmal voltage sensors (reviewed by Ríos and Pizarro, 1991; Schneider, 1994), possibly augmented by CICR (Jacquemond et al., 1991; Klein et al., 1996; Shirokova and Ríos, 1997; Stern et al., 1997; see Ríos and Stern, 1997 for a recent review). Several years ago, localized discrete calcium release events, termed "calcium sparks," were discovered using the fluorescent calcium probe fluo-3 with laser scanning confocal microscopy (M. Minsky, U.S. Patent #3013467, Microscopy Apparatus, 1957; see Inoué, 1995 for review), first in cardiac myocytes (Cheng et al., 1993; Lipp and Niggli, 1994; Cannell et al., 1994, 1995; López-López et al., 1994, 1995; see Cheng et al., 1993b for review) and later in frog skeletal muscle (Tsugorka et al., 1995; Klein et al., 1996). Generally, sparks have been interpreted as stereotyped events, whose morphology (spatial extent, duration, and amplitude) has been used to infer release flux and the number of release channels involved locally in release (Cheng et al., 1993; Cannell et al., 1994; Tsugorka et al., 1995; Klein et al., 1996; Gómez et al., 1996; Shirokova and Ríos, 1997; Blatter et al., 1997). In particular, the existence of single or multiple modes in spark amplitude histograms has been given special significance (Tsugorka et al., 1995; Klein et al., 1996; Lukyanenko et al., 1996; Shirokova and Ríos, 1997; Xiao et al., 1997; Satoh et al., 1997). However, amplitude distributions determined from confocal line scan images are distorted by a powerful sampling bias because sparks originate at variable distances from the scan line (Pratusevich and Balke, 1996; Shirokova and Ríos, 1997; Smith et al., 1998).

In this paper we first demonstrate on general grounds that the distribution of spark amplitude in line scan images must be monotonic (that is, without a mode). This generalizes the conclusion reached by Pratusevich and Balke (1996) and by Smith et al. (1998) in a more restricted case. Reported modes in amplitude histograms (Tsugorka et al., 1995; Klein et al., 1996; Lukyanenko et al., 1996; Shirokova and Ríos, 1997; Xiao et al., 1997; Satoh et al., 1997) must therefore have been caused by subjective detection bias against small amplitude events. Accordingly, we developed an automated algorithm to detect and measure sparks in line scan images without human intervention. We demonstrate the use of this algorithm in either skeletal or cardiac muscle, and confirm that the distribution of apparent amplitude (i.e., observed peak fluorescence intensity) is, in fact, nonmodal. We characterize the detection efficiency and reliability (i.e., true and false positive rates) of the algorithm on simulated line scan images. The confocal sampling theory described here may also have general applications in light and electron microscopic morphological metrics.

*Received for publication 27 May 1998 and in final form 10 November 1998.*

Address reprint requests to Heping Cheng, Ph.D., Laboratory of Cardiovascular Science, Gerontology Research Center, NIA, National Institutes of Health, 5600 Nathan Shock Drive, Baltimore, MD 21224. Tel.: 410-558-8634; Fax: 410-558-8150; E-mail: chengp@grc.nia.nih.gov.

Natalia Shirokova's permanent address is The A. A. Bogomoletz Institute of Physiology, Bogomoletz St. 4, Kiev, Ukraine.



0006-3495/99/02/606/12 $2.00

## EXPERIMENTAL METHODS

### Imaging calcium sparks in skeletal muscle

The methods used in experiments with skeletal muscle have been described in detail (Shirokova and Ríos, 1997). Briefly, segments of m. semitendinosus muscle fibers (from *Rana pipiens*, which were anesthetized in a 15% ethanol solution, then killed by pithing) were voltage-clamped in a two-Vaseline gap chamber on an inverted microscope (Axiovert 100, Zeiss, Germany) with a 40×, 1.2 N.A. water immersion objective (c-Apochromat, Zeiss). A confocal microscope attachment (MRC 1000, Bio-Rad, MA) was used to scan the fluorescence of fluo-3 (Molecular Probes, Eugene, OR) (introduced by diffusion from the cut ends) along a line parallel to the fiber axis. Images representing the scanned intensity of fluorescence, $F(x, t)$, as a function of position ($x$) along the scanned line and time ($t$), were formed by collections of 768 intensities taken at 0.139-$\mu$m distances and repeated every 2 ms. Shown are fluorescence intensity, $F(x, t)$, or fluorescence normalized to the initial intensity $F_0(x)$, obtained by averaging $F_0(x, t)$ before the depolarizing pulse.

The skeletal muscle solutions in the cut ends were "internal" (in mM): 125 cesium glutamate, 10 Cs-HEPES, 5.5 Mg $Cl_2$, 1.0 EGTA (nominal $[Ca^{2+}]$ set to 100 nM), 0.1 fluo-3, 5 creatine-phosphate, 5 ATP, and 5 glucose, pH 7.0. Separated from the cut ends by double Vaseline gaps, the "external" solutions were (in mM): 131.5 TEA-methane-sulfonate, 10 TEA-HEPES, 10 calcium methanesulfonate, TTX ($10^{-4}$ g/l), pH 7.0, 17°C.

### Cardiac calcium sparks

Ventricular cardiac myocytes were isolated from adult Sprague-Dawley rats (2–3 months old, weight 225–300 g) using standard enzymatic techniques, as described previously (Spurgeon et al., 1990). After the enzymatic treatment single cells were shaken loose from the heart and stored in HEPES buffer solution containing (in mM) 137 NaCl; 5.4 KCl; 1.2 $MgCl_2$; 1 $NaH_2PO_4$; 1 $CaCl_2$; 20 glucose, and 20 HEPES (pH 7.4). Aliquots of cells were loaded with fluo-3 by a 10-min incubation in 10 mM fluo-3 AM and then kept in the dark for up to 2 h until use.

Myocytes were imaged with a Zeiss LSM-410 inverted confocal microscope (Carl Zeiss, Inc., Germany). All image data were taken in the line scan mode, with the scan line usually oriented along the long axis of the myocyte, avoiding cell nuclei. Each image consisted of 512 line scans obtained at 2.09-ms intervals, each comprising 512 pixels spaced at 0.156 $\mu$m intervals. The microscope objective was a Zeiss Plan-Neofluar 40× oil immersion N.A. = 1.3, and the confocal pinhole was set at the setting prescribed by the manufacturer to obtain spatial resolutions of 0.4 $\mu$m in the horizontal plane and 0.9 $\mu$m in the axial direction. Image processing, data analysis, and presentation were done using the IDL software (Research Systems, Boulder, CO). Experiments were carried out at room temperature (20–22°C).

## RESULTS

### Theory of the amplitude histogram

Fig. 1 (modified from Shirokova and Ríos, 1997) plots the image of a spark, that is, the calculated intensity in image space of a centered spark, as a function of position in the $yz$ plane (orthogonal to the scanning line). The image was calculated by convolution of a Gaussian of half-width 0.7 $\mu$m (crudely representing the distribution of $Ca^{2+}$:dye complex in a spark) and a confocal response function (Art and Goodman, 1993)

$$C(v, w) = S\left[\frac{\sin(w/4)}{(w/4)}\right]^2\left[\frac{\sin(w\beta/4)}{(w\beta/4)}\right]^2\left[\frac{J_1(v)}{v}\right]^2\left[\frac{J_1(v\beta)}{v\beta}\right]^2 \quad (1)$$

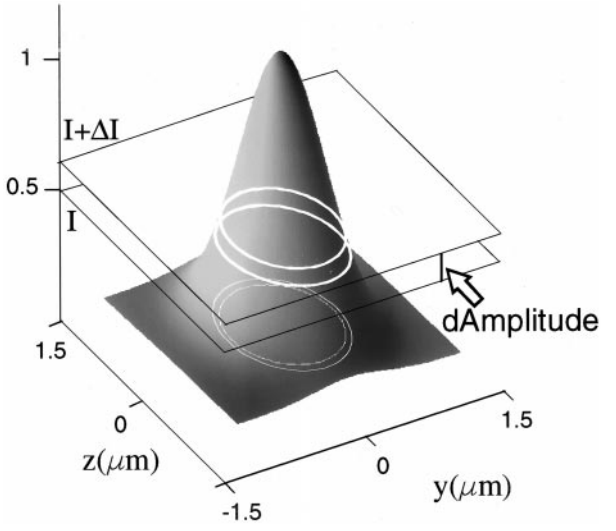


FIGURE 1 Line scan image of a spark. Theoretical image intensity profile of a spark originating at the scanned point, as a function of displacements relative to the center of calcium release in directions $y$ and $z$, perpendicular to the scanned line. As explained in the text, the graph can also be interpreted as a plot of the amplitude reported for stereotyped sparks occurring at positions $y$ and $z$ relative to the scanned line. The area of the projected annulus measures the probability density of spark amplitude, if sparks are distributed randomly in the ($yz$) plane perpendicular to the scan line. Modified from Shirokova and Ríos, 1997.

where $S$ is a scaling constant, $J_1$ is the first-order Bessel function, $\beta$ is the ratio of excitation and detection wavelengths, $w$ and $v$ are $z$ and $y$ coordinates in optical units (Art and Goodman, 1993), adjusted so that the half-widths of $C[w(z),v(y)]$ matched a measured point spread function (Pratusevich and Balke, 1996). Note that this function, which is a product of response functions in the $xy$ plane and along the $z$ axis, is only an approximation to the pointspread function of the objective, but it is used here only for illustrative purposes. Considered in object space, this function also represents the measured amplitude of a spark occurring at position ($y$, $z$) off the scanned line. Sparks are approximately equally likely to originate at any point in a Z disk (because there is no information on the location of T tubules) (Shacklock et al., 1995; Cheng et al., 1996a; Tsugorka et al., 1995; Klein et al., 1996). Thus, the cumulative amplitude distribution (frequency of measured sparks of amplitude $<I$) will be proportional to the area outside an elliptic region or resel where the intensity is $>I$ (see Fig. 1). The amplitude probability density (observed as the amplitude histogram of detected events) is proportional to the area bounded by two resels, where the amplitude increases by d*Amplitude*. Fig. 2 shows the amplitude histogram generated by the spark in Fig. 1.

Using numerical simulation and under specific assumptions on spark formation mechanism, previous studies (Pratusevich and Balke, 1996; Smith et al., 1998; Izu et al., 1998) have shown that the histogram of spark amplitudes would have no mode even if the underlying events are stereotypical. To find the general form of the amplitude

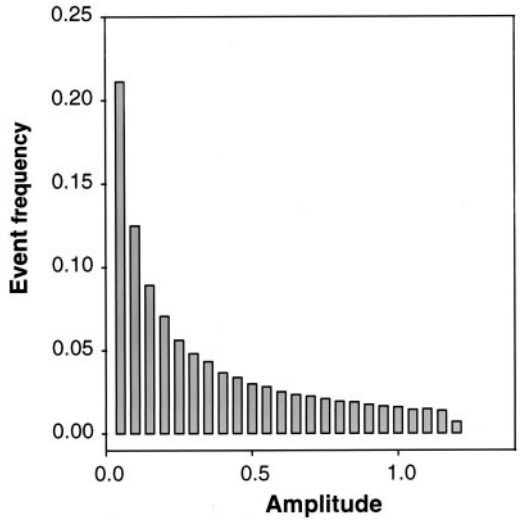


FIGURE 2 Predicted amplitude histogram in a line scan. The histogram was generated using the dependence of reported amplitude on position, shown in Fig. 2, and the assumption that sparks are generated at random locations in a Z disk. See text for details.

histogram, assume the intensity of a spark is given by a function $I(x, y, z)$. Because the scanning is along the $x$ axis, only the dependence on $y$ and $z$ needs to be taken into account. For simplicity we assume the dependency is the same for both $y$ and $z$. That is, we describe the intensity as a function $I(\rho)$, where $\rho$ is the distance from the spark center. Then, by the same argument given in Fig. 1, the number of sparks in an interval $[I, I + dI]$ of detection amplitudes will be proportional to $\rho d\rho$ (the area of the ring of radius $\rho$). The probability density function is therefore given by

$$p(I) = -A\rho(I)\frac{d\rho}{dI} \tag{2}$$

where $\rho(I)$ is the inverse function of $I(\rho)$ [existent because $I(\rho)$ is monotonic] and $A$ is a proportionality constant.

A mode in the amplitude distribution will exist if the density is increasing or

$$\frac{d}{dI}\left(\rho\frac{d\rho}{dI}\right) < 0 \tag{3}$$

which transforms to

$$\frac{dI}{d\rho} > \rho\frac{d^2I}{d\rho^2} \tag{4}$$

This is a condition on the decay of the image with distance. It states that the second derivative of the decay has to be large and negative, while the first, which is always negative, should not be too large. This says, roughly, that the spark intensity must have a region of downward (convex) curvature (see Discussion and Appendix I). Spark fluorescence is produced by diffusing chemical species originating from a presumed small source; the diffusion equation shows that diffusion will tend to dissipate such curvature except in the region of the source. Therefore, we do not expect spark fluorescence profiles, which are roughly Gaussian in shape, to satisfy Eq. 4. Convolution with the microscope pointspread function (PSF), which is also similar to a Gaussian, will not change this situation. We therefore conclude that, *if sparks originate at random positions in the plane perpendicular to the scan line, the observed amplitude histogram will be monotonically decreasing, without a mode.*

The above theoretical analysis on the global property of spark amplitude distribution assumed stereotyped sparks. Generally, if there is an arbitrary distribution for the underlying calcium release events, $g(y)$, it would be "convolved" with the nonmodal amplitude distributions characteristic of stereotyped sparks, which would not create a mode. This conclusion can be mathematically proven. Letting $f(x, y)$ be the observed amplitude distribution for a stereotypical spark corresponding to a release intensity $y$, the necessary and sufficient condition for $f(x, y)$ to be a monotonic decreasing function is that its partial derivative

$$f_x(x, y) < 0 \qquad \forall x, y > 0 \tag{5}$$

Let $F(x)$ denote the compound spark amplitude distribution, which reflects the variations in intrinsic release events intertwined by the variations due to confocal sampling. Then $F(x)$ is given by

$$F(x) = \int_0^{y_{max}} g(y)\, f(x, y)dy \tag{6}$$

Hence, its derivative $F'(x)$ is

$$F'(x) = \int_0^{y_{max}} g(y) f_x(x, y)dy \tag{7}$$

Since $f_x(x, y) < 0$ and $g(y) > 0$ for $y \in [0, y_{max}]$, we have

$$F'(x) < 0 \tag{8}$$

Equation 8 indicates that $F(x)$ a monotonic decreasing function, regardless of the exact shape of $g(y)$. A mode can appear because of the failure of the detector (human or machine) to detect sparks of small amplitude. In this case, the histogram should be left-skewed, and the location of the mode is determined by the threshold of detectability, rather than by the intrinsic properties of spark calcium release events (see Fig. 7).

## Automated spark detection algorithm

An automated spark detection algorithm was coded in the image-processing language IDL (Research Systems, Boulder, CO) (see Appendix II for a listing of the computer program). The strategy of the detection algorithm (Fig. 3) is to search for connected regions that are above the noise

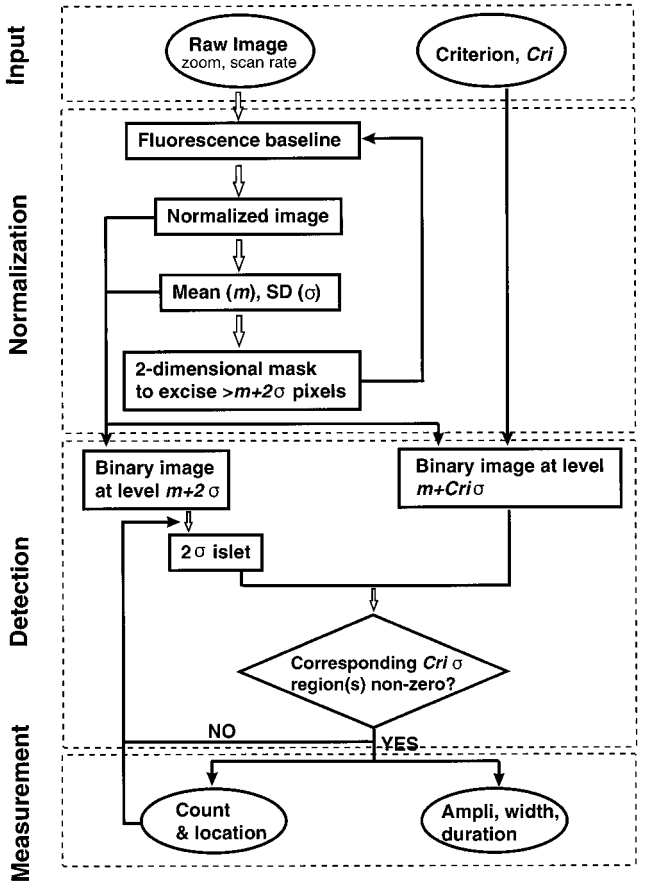


FIGURE 3 Flow chart of the spark detection and measurement algorithm. The stages of detection are described in the text. Intermediate images generated at each stage are shown in Fig. 4.

level. Tentative spark regions are located as outliers relative to the overall standard deviation of the fluorescence. These areas are then excised from the image, and the statistics of the remaining regions (presumed to have noise only) are computed again. Final spark regions are then selected by their excessive deviation from the noise distribution. To avoid the multiple counting of single sparks that have multiple peaks (because of noise), sparks are defined as connected areas that exceed a weak threshold condition, while containing some points that exceed a strong threshold. These spark areas are also used to depict spark morphology.

Fig. 3 shows the four stages in the detection algorithm. *Input:* The algorithm is fully automated; the only parameter requested from the user is a constant (*Cri* or *Cri1*) determining the "threshold" for event detection. *Normalization of image:* The spatial distribution of baseline fluorescence for normalization is first estimated by averaging all scan lines (irrespective of local or global spark activity) and then corrected by masking out potential spark regions. In the version for voltage-clamp experiments, the user may select a time interval where the baseline will be computed, so that portions with high global $[Ca^{2+}]$ can be avoided. *Event detection:* A spark is located by a pixel in which normalized fluorescence is greater than the criterion. The criterion is usually $m + Cri\ \sigma$, where $m$ and $\sigma$ refer to the mean value and standard deviation, respectively. Two binary images at levels of $m + 2\sigma$ and $m + Cri\ \sigma$ are generated. Sparks are identified as islets in the $m + Cri\ \sigma$ image and the spatio-temporal extent of each is determined by the dimensions of the corresponding islet in the $2\sigma$ image. A second criterion, $m + Cri1$, is used in voltage-clamp cases, and is explained below. In *Measurement*, lists of sparks, spatial and temporal locations, and amplitude are produced. Other measures of extent (FWHM, full width at half-maximum; FDHM, full duration at half-maximum; rise time) are also computed. Smoothing filter steps are omitted in this diagram. Fig. 4 shows the images that are generated at intermediate steps in this algorithm.

To assess the performance of the algorithm and optimize parameters for its use, we synthesized test images that consisted of an average of 35 sparks from actual experiments with cardiomyocytes, variably scaled, added to Gaussian noise whose mean and standard deviation matched those of actual line scan images. These test images were then passed through the detection algorithm to determine the number and apparent amplitude of the embedded sparks successfully detected by the algorithm, and the number of false detections in blank images containing only noise. Examples of true and false detections at different threshold levels are shown in Fig. 5.

The sensitivity of the algorithm (percent of sparks detected) and the rate of false positives are shown in Fig. 6 as a function of the amplitude of the spark for several values of the threshold criterion. In general, sensitivity decreased and specificity (100% minus percent of detections that are false) increased with increasing threshold, as expected. For a direct comparison, we also tested the sensitivity and reliability of eye detection. The result suggests that detection by "well-trained" eyes has a sensitivity comparable to the computer detection at $Cri = 3.8$, but with higher reliability (Fig. 6). Because detectability increases with amplitude, the use of a more stringent criterion produces greater undercounting at low amplitudes, creating an apparent mode in the detected amplitude histogram whose position moves rightward (to higher amplitudes) as the detection criterion becomes more stringent (Fig. 7). However, because of the presence of noise, some low amplitude sparks may be detected while others of higher amplitude are missed. Furthermore, because of the interaction of noise with the complicated nonlinearity of the algorithm, the estimated amplitude of sparks differs from the true amplitude (i.e., the amplitude estimation is biased), by an amount that depends inversely on the amplitude (Fig. 8), so that the amplitude of small sparks is over-reported.

It is noteworthy that at a given signal-to-noise ($m/\sigma$) level, the rate of false detection (type I error) depends largely on the *Cri*. However, $m/\sigma$ is an important determinant for the magnitude of erroneous rejection (type II error). Using the amplitude-scaled averaged sparks as the test objects (of a stereotyped shape but variable intensities), this

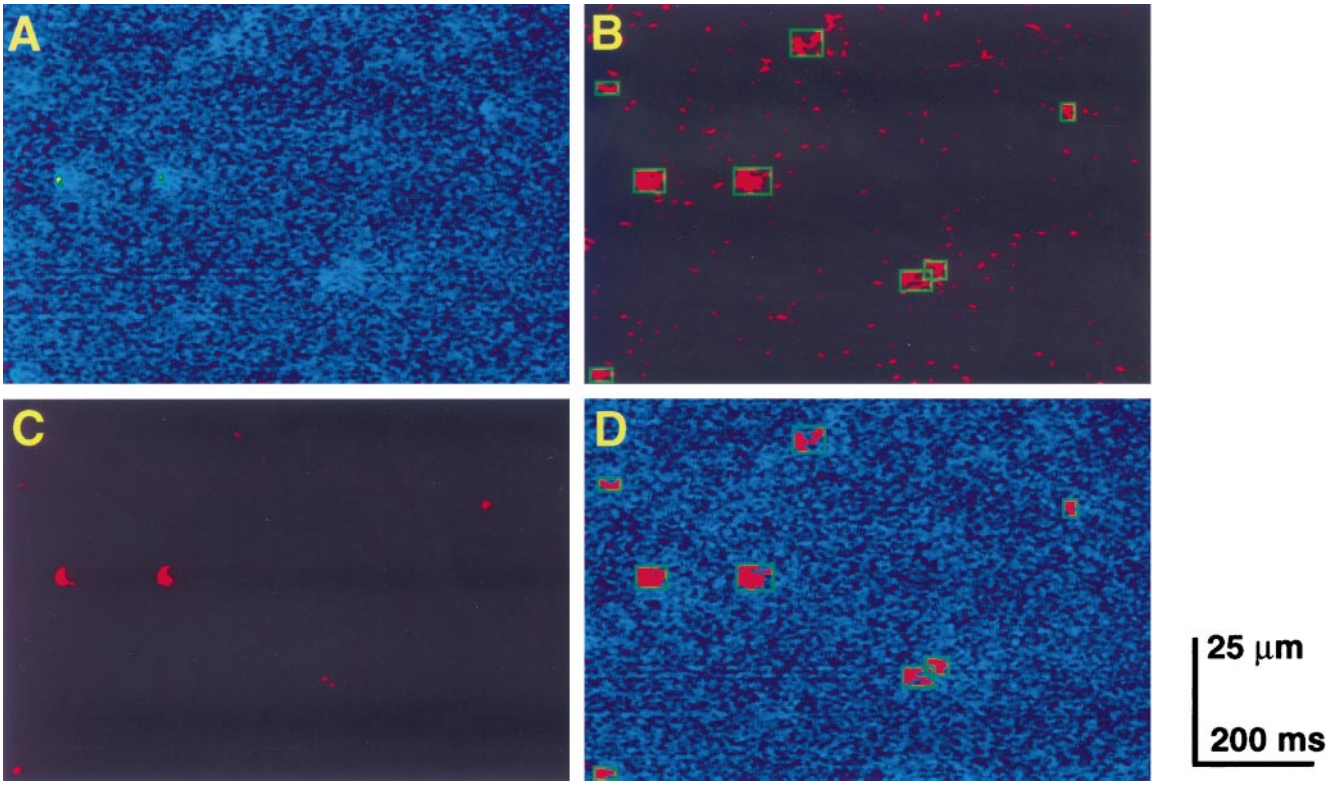


FIGURE 4 Intermediate outputs of the algorithm. (*A*) Normalized line scan confocal image of spontaneous calcium sparks. (*B*) Binary images for regions above (*1, red*) or below (*0, black*) $m + 2\sigma$. (*C*) Binary image at level of $m + Cri\ \sigma$ ($Cri = 3.8$). Detected spark events are marked by boxes in (*B*). (*D*) Detected events and fluorescence image.

analysis shows that $Cri = 3.5$ is close to ideal at $m/\sigma = 3.0$, in the sense of providing high sensitivity and reliability at the same time.

## Modified algorithm for use under voltage clamp in skeletal muscle

Under voltage clamp conditions, particularly in skeletal muscle, the nature of the raw image data is altered in two ways. First, during the active clamp step, there may be a smooth elevation of background fluorescence (Fig. 9), because of abundant out-of-line release events, or to continuous release or release in unresolvable small events (Shirokova and Ríos, 1997). Second, there is a time interval before the start of the active clamp during which this time-varying background is known to be absent. Additionally, the resting fluorescence has notable periodic variations, coincident with sarcomeric repeats. For these conditions, the algorithm was modified (Fig. 10). The resting fluorescence $F_0(x)$ was determined as a time average of the image fluorescence $F_0(x, t)$ during the rest period before the pulse, and used for normalization. Sparks were then tentatively located and excised from the image, after which a time- and space-varying average fluorescence during the active period was computed. The final selection of sparks was made by a criterion of excess intensity over this varying background, usually by an absolute amount (in units of $\Delta F/F_0$), rather than relative to the standard deviation of the background. The human participation was again limited to setting a threshold.

The use of an absolute threshold criterion was warranted because $\sigma$ changed with release intensity and global $[Ca^{2+}]$, which increased during a depolarizing pulse. It changed with release intensity presumably because of out-of-focus sparks and nonspark release. It changed with $[Ca^{2+}]$ because fluorescence increases with $[Ca^{2+}]$, and "background" noise should largely follow Poissonian photon emission, $\sigma^2 = N$, where $N$ refers to number of photons per pixel. Under these conditions, particularly when the spark frequency is high, use of a relative criterion, $Cri\ \sigma$, implied widely different criteria for sparks at different voltages and even during a single pulse. It should be noted that the computations before the final selection, which are integral components of the algorithm, are essentially the same in the two versions of the spark detector. Both versions performed equally well when the spark frequency was $<40$ per image and $\sigma$ did not change by more than twofold in a single image (data not shown).

## The amplitude distribution of detected sparks has no mode

An amplitude histogram of 127 sparks obtained from the same skeletal muscle fiber held at $-65$ mV (Fig. 11 *A*)

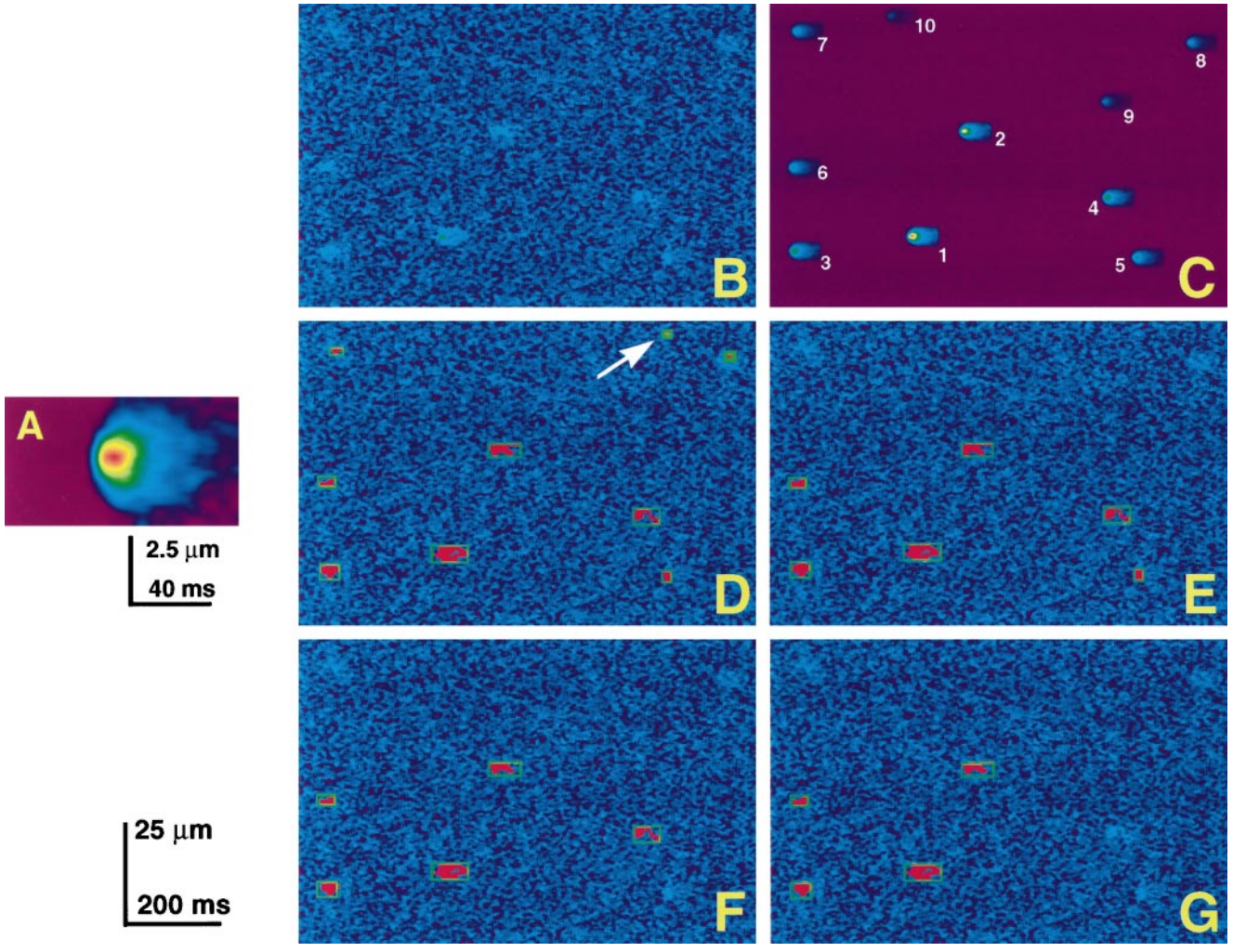


FIGURE 5 Assessment of algorithm performance. (*A*) Average of 35 sparks used as test object ("standard spark"). (*B*) Test images formed adding the standard spark at variably scaled intensity to background Gaussian noise with mean $m = 30$ and standard deviation $\sigma = 10$. (*C*) Location and relative intensity of sparks shown in (*B*). Labels 1 to 10 refer to sparks of $\Delta F/F_0 = 0.6, 0.5, 0.4, 0.38, 0.3, 0.28, 0.25, 0.15, 0.2$, and 0.1. (*D–G*) Sparks detected at $Cri = 3.5$ (*D*), 3.8 (*E*), 4.2 (*F*), and 4.8 (*G*). There are 9, 6, 5, and 4 events detected in *D–G*, respectively. The arrow in (*D*) indicates a false detection. Because of the presence of noise, detected sparks (e.g., #6 in *F*, #7 in *G*), may be dimmer than the ones that went undetected (e.g., #5 in *F*, #4 in *G*).

showed no evidence of a mode, consistent with the theoretical prediction above. In a larger set of image data obtained in cardiac myocytes ($n = 38$ cells), although a mode was observed, its position moved rightward as the detection criterion was made more stringent, and importantly, the mode was always located near the 50% detection amplitude. As shown in Figs. 6 and 7, at $Cri = 4.8, 4.2, 3.8$, and 3.5, the 50% detection $\Delta F/F_0$ level was 0.43, 0.39, 0.34, and 0.31 (Fig. 6), respectively, while the mode occurs at 0.45, 0.40, 0.35, 0.30 (Fig. 7), respectively. Moreover, at $Cri = 3.5$, the amplitude histogram of 2010 detected events was highly leftward skewed, and was monotonically decreasing except at the very left end, where the detectability is extremely small (Figs. 6 and 7). Thus, the observed histograms are perfectly consistent with the idea that the ideal observed amplitude distribution (i.e., in noise-free conditions) would be nonmodal. As shown theoretically above, this distribution cannot be taken as evidence that the underlying calcium release events are heterogeneous; such a monotonic amplitude distribution would be expected even if the underlying events were perfectly stereotyped. However, we found that there was a low positive correlation among spark amplitude, duration, and width (Fig. 11, *B* and *C*, consistent with previous data on cardiac sparks (Song et al., 1997). This strongly suggests that there is a real variation in the characteristics of sparks, rather than just a difference in their position relative to the scan line, because width should be negatively correlated with amplitude if both were determined by a single random variable (distance from scan line). Given that there is an intrinsic variation in underlying release events, weak sparks can be produced not only by off-center sampling, where the spatiotemporal spreading is expected to be more diffusive, but also by small release events, where the spreading might be expected to be more

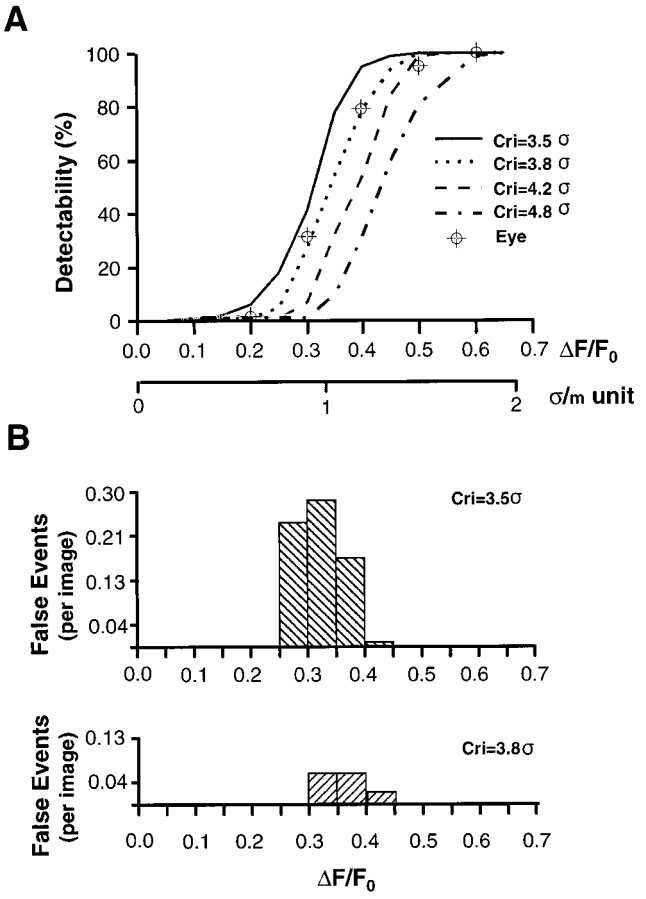


FIGURE 6 Sensitivity and reliability. (*A*) "Sensitivity" or "detectability" (percent of sparks detected) versus spark amplitude at different criteria. The average results of eye detection by two coauthors (H.C. and L.S.) are shown by the crossed circles. The abscissa is plotted in both $\Delta F/F_0$ and $\sigma/m$ (normalized noise level) units. Data were derived from the synthetic test images (see text). (*B*) Reliability test. Rate of false detections were estimated from 120 blank images of 512 × 512 pixels, with noise regenerated for every image. False detection events per image were shown for *Cri* = 3.5 (*top*) or 3.8 (*bottom*). There are totals of one and none false events at *Cri* of 4.2 and 4.8, respectively (not shown). As the threshold is increased, reliability increases and sensitivity decreases. No false positives were detected by eye in the reliability test.

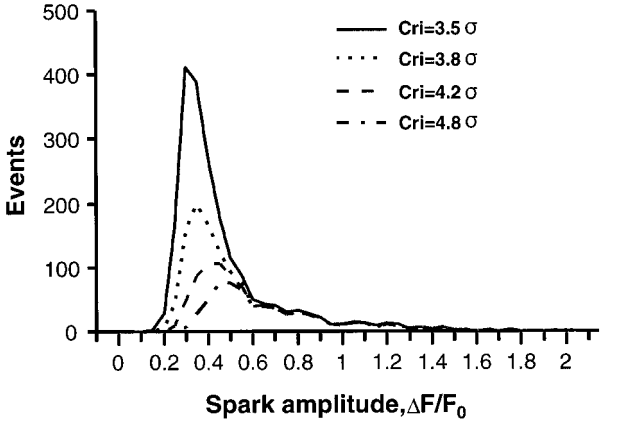


FIGURE 7 Amplitude distribution of cardiac calcium sparks. 2010, 1204, 847, or 632 spontaneous events were detected from 38 cells at *Cri* = 3.5, 3.8, 4.2, or 4.8. Reducing the criterion underscores the monotonically decaying character of the distribution. (False events were expected to be 206 or 10% at *Cri* = 3.5, 43 or 3% at *Cri* = 3.8, 1 or 0.3% at *Cri* = 4.2, and 0% at *Cri* = 4.8).

confined in space and time. For this reason, the linear correlation analysis may not be used to infer quantitative relations among spark parameters.

## DISCUSSION

Calcium sparks provide a unique window on the local processes of excitation-contraction (EC) coupling. It is widely expected that they will help distinguish between different theories of the EC coupling process, and that their properties will help determine how EC coupling is deranged in pathophysiologic states such as myocardial hypertrophy, heart failure, and malignant hyperthermia. To fulfill this promise, it will be necessary to resolve such deceptively simple questions as how many release channels are involved in the production of sparks, whether the time course and/or amplitude of sparks is stereotyped, and how the spark release flux depends on physiologic variables such as SR calcium load. Unfortunately, the optimum method for detecting sparks, confocal fluorescence microscopy in line scan mode (Cheng et al., 1993), inherently produces a complicated distortion of the amplitude of sparks because of the deviation of their centers from the confocal scan line (Cheng et al., 1993; Pratusevich and Balke, 1996; Shirokova and Ríos, 1997; Smith et al. 1998; this study). We have shown theoretically and confirmed experimentally that sparks, as observed through line scans, have a monotonically decreasing amplitude distribution, regardless of whether the underlying events are stereotyped or not. Thus, to infer the nature of calcium sparks, it is important to take

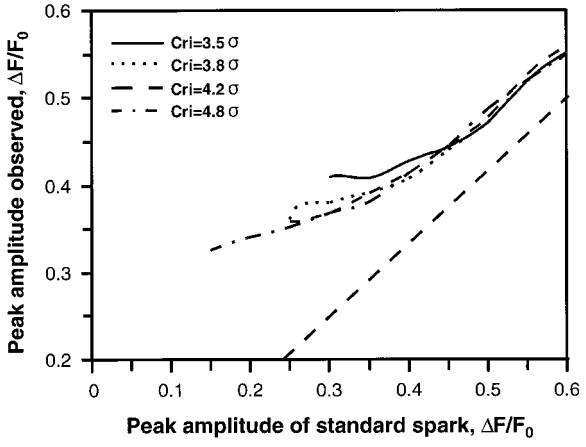


FIGURE 8 Noise and measurement of spark amplitude. Observed versus true spark amplitude. *Dashed straight line:* measured spark amplitude in the absence of noise, which is 16% smaller than the true peak because of smoothing steps in our algorithm. Spark amplitude is increased by noise, in particular for faint sparks. Note also the nonlinear relationship between detected and true spark amplitude at low amplitudes. Data were derived from the synthetic test images (see text).

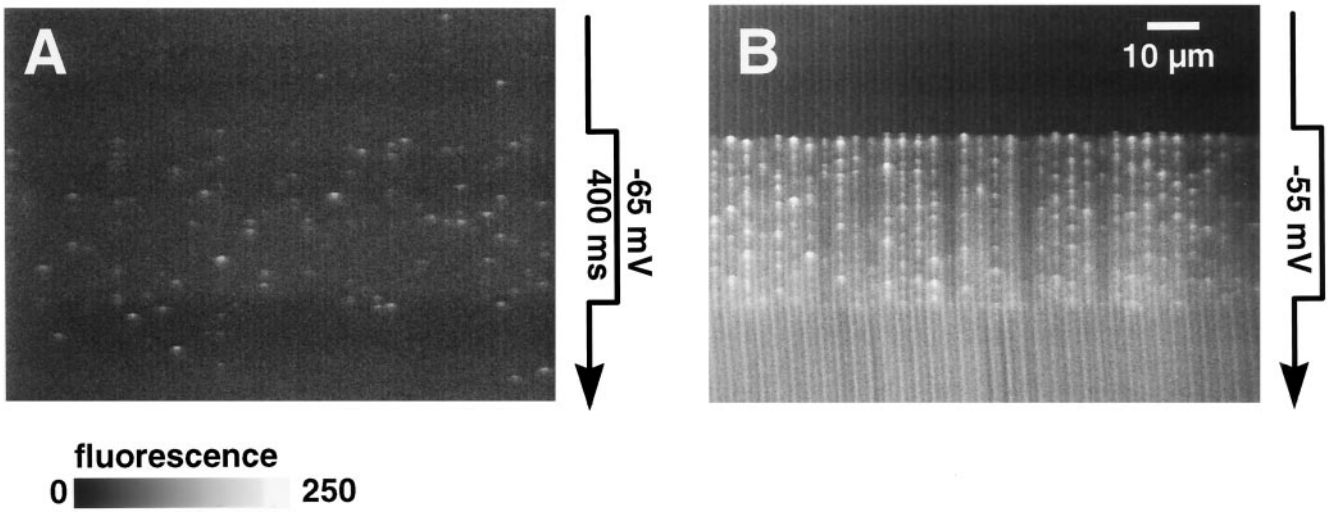


FIGURE 9 Problems with sparks elicited by voltage clamp. In voltage clamp experiments in frog semitendinosus, sparks can be very close together, and there is often release not in the form of sparks (Shirokova and Ríos, 1997). Under our experimental conditions (e.g., inclusion of EGTA), sparks are always briefer and often narrower than in cardiac muscle. (*A*) Fluorescence in a skeletal muscle fiber upon stimulation at a low voltage (−65 mV). (*B*) At a higher voltage (−55 mV) in a different cell. The images present clearly different resting and active intervals, the latter corresponding to the time of the depolarizing pulse.

into account confocal sampling theory in the context of specific statistical models of the spark generation process. This makes it all the more important that the method of detection be objective, and be capable of automated use to count large numbers of sparks (to yield robust statistics). We have developed, tested, and implemented such an algorithm here. We found that our algorithm can be operated so as to detect 50% of the sparks of size of 0.31 $\Delta F/F_0$ unit, which is approximately one unit of the scaled standard deviation of the background noise ($\sigma/m = 0.33$) (Fig. 6). When applied to cardiac myocytes, it produced only 10% false positive detection, i.e., 90% specificity (Fig. 7). By using this algorithm, we find nearly twice as many sparks as are counted by eye (data not shown; Song et al., 1997).

Since false positives are biased toward small amplitudes (see Fig. 6 *B*), it might be argued that the increased number of small events detected by the automatic detector is the result of false positives. However, our results suggest that this is unlikely the case. As shown in Fig. 7, at $Cri = 3.8$, there are 411 events detected at $\Delta F/F_0$ interval [0.25, 0.35]. Assuming that 73% (Fig. 6 *B*) of the estimated false positives (150 of 206 events, see Fig. 7 legend) is in this $\Delta F/F_0$ range, there should be 261 true spark events after correction for false detection, higher than the (uncorrected) modes at $Cri = 3.8$ (199), 4.2 (106), or 4.8 (78). If we further take the detectability (~0.5 at $\Delta F/F_0 = 0.3$) into account, there should have been 520 sparks in this $\Delta F/F_0$ range; that is, the number of observed events (411) only *underestimates* the number of true sparks. Thus, based on the demonstrated reliability of the method, we can be reasonably confident that these additional sparks, missed by human observers, are real. The inclusion of these events, which are mostly of small amplitude, reveals the nonmodal amplitude distribution predicted by theory. This shows that counting by human observers is not only inefficient, but introduces overwhelming bias into the distribution of spark properties. In particular, the abscissa of modes found in human-counted amplitude histograms turns out to be of very little value. The most reliable information is instead in the amplitude of the large sparks in an image, which may be interpreted as being both large (as object sparks) and in-focus. The significance of this detected amplitude depends on whether the object sparks are narrowly distributed, in which case the detected amplitude is representative of true modal amplitude, or widely distributed, in which case the large detected amplitudes can only be interpreted as outliers.

It should be pointed out that there are hypothetical and special experimental situations when a modal amplitude distribution for stereotypical spark events could be observed. 1) We show in Appendix I that it is possible to specify any amplitude histogram, including one with modes, and then construct a (hypothetical) spark intensity profile that would give rise to the specified amplitude histogram. However, the intensity profiles (or PSF) required to produce histograms with modes are not realistic (Fig. 12). 2) Theoretically, artifactual multimodal amplitude distribution could be obtained if the release sites formed a regular lattice, as shown by Pratusevich and Balke (1996) in their numerical simulation. But this is also unlikely to occur inside the cells. Nevertheless, there are special experimental conditions conducive to a modal distribution of a stereotypical event. 3) Let $A(r)$ be the relationship between the detected amplitude of a spark ($A$) and the distance from where it originates to the scanned region ($r$). In a nutshell, the reason why there are no modes in a *line scan* image is that the volume of space at a given distance increases with the square power of the distance to the scanned line; thus the frequency of sparks increases very rapidly as their detected

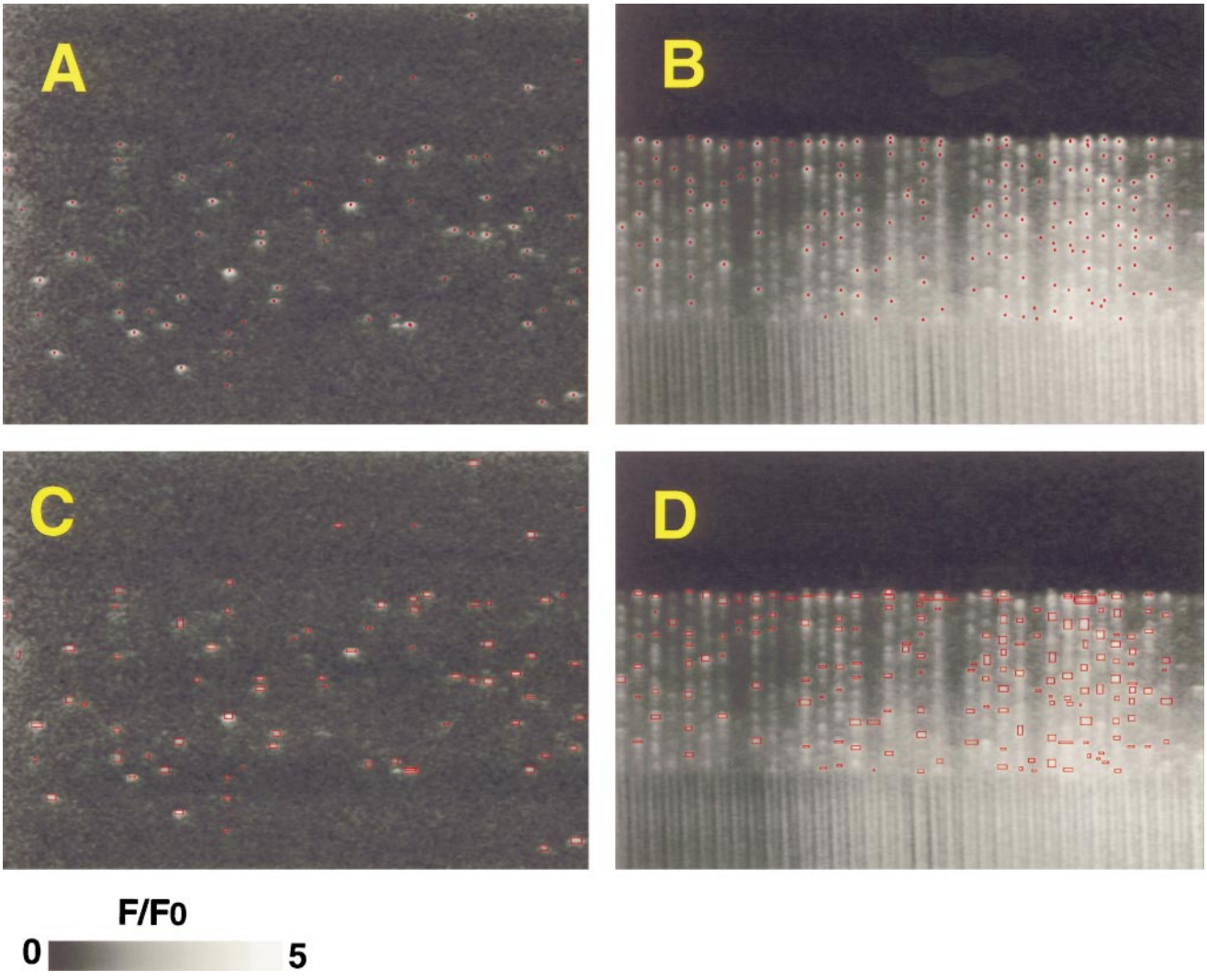


FIGURE 10 Criteria for sparks under voltage clamp. The program required two modifications: (I) Resting fluorescence [$F_0(x)$] is calculated as an average over the resting interval. (II) Sparks are located as regions exceeding a normalized fluorescence $f(x)$, averaged during the active interval excluding the spark regions, by either *Cri* $\sigma$ (the relative criterion) or *Cri1*. (*A* and *B*) Fluorescence in Fig. 9 after normalization and digital filtering, with red dots at spark maxima, placed by the spark locator with *Cri1* = 0.4. Note that the apparently undetected events are all below 0.4 units when selected and measured directly. The choice of threshold is constrained by the opposing requirements of reliability and sensitivity. We chose a higher threshold to avoid false detections (with the penalty of erroneous rejection of true events) and show that even under these conditions, the skeletal muscle spark amplitude exhibits a monotonic decreasing histogram distribution. (*C* and *D*) Rectangles mark FWHM and FDHM.

size decreases. In a *time-resolved xy scan* image instead, the volumes of space increases linearly with distance to the focal plane. Thus it can be demonstrated, for perfectly stereotyped sparks, that the detected amplitude distribution in an *xy* scan would have a mode provided that the *z* axis PSF had an inflection point. 4) Finally, a modal distribution can be observed if the assumption of random sampling is violated and if spark amplitude is truly modal, e.g., small sample statistics in conjunction with punctuated distribution of spark origin, or statistics for sparks originating from the same, repetitively active sites (Cheng et al., 1993; Xiao et al., 1997; Parker and Wier, 1997; Klein et al., 1998).

Finally, it may be instructive to highlight some important features of our algorithm (Fig. 3 and Appendix II). Taking both spatial and temporal properties of calcium sparks into account, detection involves the following array-oriented computations: masking, spatiotemporal filtering, and connectivity in the *x-t* images. The spatial and temporal filters, with extents based upon the FWHM and FDHM characteristics of calcium sparks, were used at various stages of data processing, to reject local extremes, to yield local average, and to reject single pixels or small islets in the raw *Cri* $\sigma$ binary masks. Thus, the decision rules involve a sequence of computations rather than a simple threshold method. The use of the relative criterion ($m$ + *Cri* $\sigma$) appears to be convenient when the event density is low, and the global [$Ca^{2+}$] does not increase, as it ensures that higher absolute thresholds are used for noisy images, so the number of false positives per image (type I error) remains the same. It proved, however, inconvenient in situations when $\sigma$ is non-

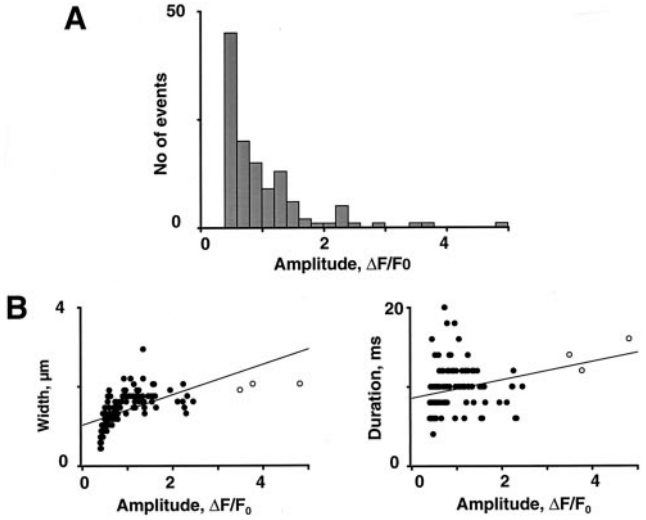


FIGURE 11 Amplitude histograms have no mode. (*A*) Amplitude histogram of 127 events found in the image in Fig. 10 *A* and another image obtained in the same fiber at the same voltage. In agreement with expectations, there is no evidence of modes. (*B*) Amplitude versus width, and amplitude versus duration, showing a small positive correlation among all three measures. This indicates that there is a real distribution of spark sizes (sparks are different in amplitude, not just detected differently). Open symbols in each scatter plot are the three largest sparks in the histogram. Because they are not especially wide, or prolonged in duration, they are probably closest to the focal plane of the microscope.

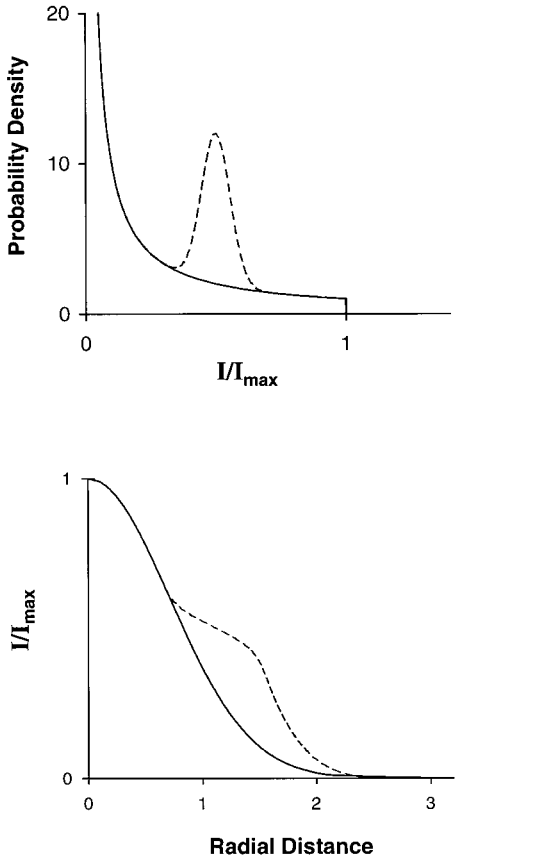


FIGURE 12 Hypothetical spark amplitude distributions (*top*) and the spark intensity profiles that generate them (*bottom*). The solid curve in the bottom panel shows a Gaussian spark intensity profile, which gives rise, by Eq. 2 (see text) to an amplitude distribution proportional to 1/*amplitude* (*top panel, solid curve*). By adding a Gaussian term to this distribution, a distribution with a mode near $I_{max}/2$ is created (*top panel, dashed curve*). Back-calculation using Eq. 10 from Appendix I then shows that the spark intensity profile required to produce this modal distribution (*bottom panel, dashed curve*) has a shoulder near the half-amplitude point.

stationary because of local variations in release intensity and background [$Ca^{2+}$]. In those cases we opted for an absolute criterion, as the relative one would result in wide variations of threshold within the same image and unacceptable increases in the number of undetected events (type II error). With its inherently array-oriented design, our algorithm is also readily applicable to calcium spark data obtained by the time-resolved *xy* scan technique (e.g., Tanaka et al., 1997). However, a more advanced algorithm could be developed, explicitly making use of other spatial and temporal properties of the spark. Certainly, human observers, make use of such cues—"you know one when you see one." It should be relatively easy to use, for example, their "funnel" appearance in line scan images. In developing such improvements it is possible, however, to introduce new sources of bias, particularly since the release process and reaction-diffusion interactions that produce the spark are incompletely understood at present (see Smith et al., 1998; Izu et al., 1998).

## APPENDIX I

### Construction of a spark fluorescence profile that generates a specified amplitude histogram

Taking the reciprocal of Eq. 2 gives a differential equation for the spark intensity profile $I(\rho)$:

$$\frac{dI}{d\rho} = -\frac{A\rho}{p(I)} \tag{9}$$

This equation can be formally integrated to give the (implicit) solution:

$$\int_{I}^{I_{max}} p(i)\, di = \frac{\rho^2}{R^2} \tag{10}$$

where $A$ and the constant of integration have absorbed into the values $I_{max}$, the peak intensity of the spark (at $\rho = 0$), and $R$, the spark radius (at which $I = 0$). Given any proposed amplitude histogram $p(i)$, the integral can be performed and Eq. 10 solved for $I$ as a function of $\rho$, giving the spark profile which would generate that histogram. One case of particular interest is the Gaussian spark profile, which gives rise to the monotonic distribution $p(I) = 1/I$ for $I < I_{max}$. This may be verified most easily using Eq. 2. Adding a (normally distributed) peaked component to this distribution gives rise, via Eq. 10, to a "spark" profile with a hump on its descending limb (Fig. 12). In general, a mode in the amplitude histogram corresponds to a shoulder in the spark intensity profile. Clearly, such intensity profiles will not be produced by a diffusion process whose source is small compared to the diameter of the PSF of a properly aligned microscope.

## Appendix II
## Codes for automatic spark detector

```
;parameter input

tscan=2.0913                    ;ms per line
ZOOM=4.                         ;zoom set
psize=0.625/zoom                ;0.625 um per pixel when zoom=1
black=10                        ;used for cell edge detection. Cell region>black
human=0                         ;user interface 1=active, other=inactive
crii=[3.5,3.8,4.2,4.8]          ;criteria for spark region folds of SD above mean

for ccrit=0,3 do begin
cri=crii[ccrit]

;input of image data

y=read_tiff('c:\image\062597\a000.tif')
ima=y
imal=y

;setup display windows

a=size(ima)&nx=a(1)&ny=a(2)
window,3,xs=nx,ys=ny            ;for cri*SD binary image
window,1,xs=nx,ys=ny            ;for 2SD binary image
window,2,xs=nx,ys=ny            ;for original normalized image only
window,0,xs=nx,ys=ny            ;for original normalized image overlayed with 2SD sparks

;setup LUT

loadct,0
tvlct,r,g,b,/get
r[220]=255&g[220]=0&b[220]=0    ;red for spark region
tvlct,r,g,b

;iterative computation of variance or SD

ima=float(median(ima,5))
                                ;minimal median filter to remove data points at extremes
imm=ima                         ;keep a copy to be used later
ss=(0.8/psize)&st=(10./tscan)&ct=0&imb=fltarr(nx,ny)
                                ;0.8-um and 10-ms spatiotemproal smoothing filter
for ia=-fix(ss/2),fix(ss/2) do begin &imb=imb+shift(ima,ia,0)&ct=ct+1&endfor
for ib=-fix(st/2),fix(st/2) do begin &imb=imb+ shift(ima,0,ib)&ct=ct+1&endfor
ima=imb/ct
imb=ima
a=rebin(ima,nx,1)&a=where(a gt black)&pl=min(a)&pr=max(a)
                                ;cell edges detected and then stored as pl and pr
ima=ima/rebin(rebin(ima,nx,1),nx,ny)
                                ;initial normalization
sd=stdev(ima(pl:pr,*))          ;inital estimate SD of the image data

mask=bytarr(nx,ny)&mask(where(ima gt 1+1.5*sd))=1&mask=median(mask,5)
                                ;mask for potential spark regions >m+1.5SD
ima=imb*(1-mask)                ;excise potential spark regions
base=smooth(rebin(ima,nx,1)/rebin(1.-float(mask),nx,1),3,edge=1)
                                ;calculate baseline with potential spark regions excised
imb=imb/rebin(base,nx,ny)       ;normalization using corrected baselins
tem=imb(pl:pr,*)*(1.-mask(pl:pr,*))
                                ;corrected background SD
sd=stdev(tem(where(tem gt 0.)),mean)

;Spark detection

im=median(fix((imb-(1.+cri*sd)>0)*100000.<1),5)
                                ;binary image of  cri*SD, spark sites
                                ;median filter to reject subsize islets and
                                ;single pixels in the raw cri*SD binary image
im(0:ss/2,*)=0&im(nx-ss/2-1:*,*)=0&im(*,0:st/2)=0&im(*,ny-st/2-1:*)=0
                                ;take care the edge effect of the smoothing
ime=median(fix((imb-(1.+2.0*sd)>0)*100000.<1),5)
                                ;2SD image for automated regional counting
ime(0:ss/2,*)=0&ime(nx-ss/2-1:*,*)=0&ime(*,0:st/2)=0&ime(*,ny-st/2-1:*)=0
imf=ime
imb=imm/rebin(base,nx,ny)       ;imb will be used for spark measurement

wset,0&tv,(imb-.5>0)*150<250    ;display the normalized image with contrast enhanced

wset,2&tv,(imb-.5>0)*150<250
wset,3&tvscl,im                 ;cri*SD image
wset,1&tvscl,ime                ;2-SD image

skc=0                           ;initalize spark counter

jump1: ime=imf

While (total(im) ne 0) do begin
a=min(where(im eq 1))
tt=a/nx&xx=a mod nx

    ;define search area
nnl=fix(min([4./psize, xx]))
nnr=fix(min([4./psize, nx-xx-1]))
mmb=fix(min([250./tscan, tt]))
mme=fix(min([250./tscan, ny-tt-1]))
ym=bytarr(nnl+nnr+1,mmb+mme+1)  ;array to hold growing points
ym(nnl,mmb)=1                   ;initial seeding for growth
sk=ym                           ;array to hold  the spark as seen in the 2SD image

for iii=0,500 do begin          ;surface growth generation count
yt=sk
          ;potential new surface points
yn=(ime(xx-nnl:xx+nnr,tt-mmb:tt+mme)) and fix(smooth(float(ym),3,edge=1)*100.<1)
                                ;dilation of ym by 3*3 filter
if total(yn) eq 0 then goto, jump2
                                ;no furth growth, stop and update spark count

sk=sk>yn                        ;update sk
ime(xx-nnl:xx+nnr,tt-mmb:tt+mme)=ime(xx-nnl:xx+nnr,tt-mmb:tt+mme)-fix(sk)>0
                                ;excise the points that already included in the cluster
im(xx-nnl:xx+nnr,tt-mmb:tt+mme)=im(xx-nnl:xx+nnr,tt-mmb:tt+mme)-fix(sk)>0
ym=yn-fix(yt)>0                 ;true new surface growth point
if iii eq 500 then print,'WARNING: SPARK SEARCH AREA MAY BE TOO SMALL'
endfor

jump2:skc=skc+1
endwhile

;Optional user interface

old_font = !p.font              ;use hdw font
!p.font = 0

while human eq 1 do begin
wset,0                          ;activate image window
print,'click left button at a spark to be discarded'
print,'middle button to add a spark'
print,'right button to exit'
cursor,ix,iy,3,/dev
if !err eq 4 then goto, jump4
if (!err  eq 1) then begin
repeat cursor,ix,iy,0,/dev until !err eq 0
for i=1,skc do begin
if (ix le s(13,i) and ix ge s(12,i)) and (iy le s(15,i) and iy ge s(14,i)) then begin
    ;update window
wset,2&xu=tvrd(s(12,i),s(14,i),s(13,i)-s(12,i)+1,s(15,i)-s(14,i)+1)
wset,0&tv,xu,s(12,i),s(14,i)
skc=skc-1
print, 'spark ',i,' has been deleted'
endif
endfor
endif
if (!err eq 2)and (imf(ix,iy) eq 1) then begin
im(ix,iy)=1
print,'spark',skc+1,'will be added'
goto,jump1
endif
endwhile

jump4: print, 'number of sparks detected at cri=', cri, 'is', skc
endfor
end
```

The authors thank Harold Spurgeon and Bruce Ziman for technical support and Amelia Morani for critical reading of this manuscript.

This work was supported by National Institutes of Health (NIH) intramural research programs (to H.C., E.G.L., and M.D.S.); by grants from the NIH and the Muscular Dystrophy Association (to E.R.); and an NIH grant (to N.S.). A.G. was the recipient of a Senior Fellowship from the American Heart Association of metropolitan Chicago.

## REFERENCES

Art, J. J., and M. B. Goodman. 1993. *In* Cell Biological Applications of Confocal Microscopy. B. Matsumoto, editor. Academic Press, Inc., New York. 47–77.

Blatter, L. A., J. Huser, and E. Ríos. 1997. Sarcoplasmic reticulum $Ca^{2+}$ release flux underlying $Ca^{2+}$ sparks in cardiac muscle. *Proc. Natl. Acad. Sci. U.S.A.* 94:4176–4181.

Cannell, M. B., H. Cheng, and W. J. Lederer. 1994. Spatial nonuniformities in $[Ca^{2+}]_i$ during excitation-contraction coupling in cardiac myocytes. *Biophys. J.* 67:1942–1956.

Cannell, M. B., H. Cheng, and W. J. Lederer. 1995. The control of calcium release in heart muscle. *Science*. 268:1045–1049.

Cheng, H., W. J. Lederer, and M. B. Cannell. 1993. Calcium sparks: elementary events underlying excitation-contraction coupling in heart muscle. *Science*. 262:740–744.

Cheng, H., M. R. Lederer, W. J. Lederer, and M. B. Cannell. 1996a. Calcium sparks and $[Ca^{2+}]_i$ waves in cardiac myocytes. *Am. J. Physiol.* 270:C148–C159.

Cheng, H., M. R. Lederer, R.-P. Xiao, A. M. Gómez, Y.-Y. Zhou, B. Ziman, H. Spurgeon, E. G. Lakatta, and W. J. Lederer. 1996b. Excitation-contraction coupling in heart: new insights from $Ca^{2+}$ sparks. *Cell Calcium.* 20:129–140.

Fabiato, A. 1985. Simulated calcium current can both cause calcium loading in and trigger calcium release from the sarcoplasmic reticulum of a skinned canine cardiac Purkinje cell. *J. Gen. Physiol.* 85:291–320.

Gómez, A. M., H. Cheng, W. J. Lederer, and D. M. Bers. 1996. $Ca^{2+}$ diffusion and sarcoplasmic reticulum transport both contribute to $[Ca^{2+}]_i$ decline during $Ca^{2+}$ sparks in rat ventricular myocytes. *J. Physiol. (Lond).* 496:575–581.

Inoué, S. 1995. Foundations of confocal scanned imaging in light microscopy. *In* Handbook of Biological Confocal Microscopy. J. B. Pawley, editor. Plenum Press, New York. 1–17.

Izu, L. T., W. G. Wier, and C. W. Balke. 1998. Theoretical analysis of the $Ca^{2+}$ spark amplitude distribution. *Biophys. J.* 75:1144–1162.

Jacquemond, V., L. Csernoch, M. G. Klein, and M. F. Schneider. 1991. Voltage-gated and calcium-gated calcium release during depolarization of skeletal muscle fibers. *Biophys. J.* 60:867–873.

Klein, M. G., H. Cheng, L. F. Santana, Y. H. Jiang, W. J. Lederer, and M. F. Schneider. 1996. Two mechanisms of quantized calcium release in skeletal muscle. *Nature*. 379:455–458.

Klein, M. G., A. Lacampagne, and M. F. Schneider. 1998. A repetitive gating mode of $Ca^{2+}$ sparks in skeletal muscle fibers. *Biophys. J.* 74:269*a*. (Abstr.).

Lipp, P., and E. Niggli. 1994. Modulation of $Ca^{2+}$ release in cultured neonatal rat cardiac myocytes. Insight from subcellular release patterns revealed by confocal microscopy. *Circ. Res.* 74:979–990.

López-López, J. R., P. S. Shacklock, C. W. Balke, and W. G. Wier. 1994. Local, stochastic release of $Ca^{2+}$ in voltage-clamped rat heart cells: visualization with confocal microscopy. *J. Physiol. (Lond).* 480:21–29.

López-López, J. R., P. S. Shacklock, C. W. Balke, and W. G. Wier. 1995. Local calcium transients triggered by single L-type calcium channel currents in cardiac cells. *Science*. 268:1042–1045.

Lukyanenko, V., I. Györke, and S. Györke. 1996. Regulation of calcium release by calcium inside the sarcoplasmic reticulum in ventricular myocytes. *Pflugers Arch.* 432:1047–1054.

Parker, I., and W. G. Wier. 1997. Variability in frequency and characteristics of $Ca^{2+}$ sparks at different release sites in rat ventricular myocytes. *J. Physiol. (Lond).* 505:337–344.

Pratusevich, V. R., and C. W. Balke. 1996. Factors shaping the confocal image of the calcium spark in cardiac muscle cells. *Biophys. J.* 71: 2942–2957.

Ríos, E., and G. Pizarro. 1991. Voltage sensor of excitation-contraction coupling in skeletal muscle. *Physiol. Rev.* 71:849–908.

Ríos, E., and M. D. Stern. 1997. Calcium in close quarters: microdomain feedback in excitation-contraction coupling and other cell biological phenomena. *Annu. Rev. Biophys. Biomol. Struct.* 26:47–82.

Satoh, H., L. A. Blatter, and D. M. Bers. 1997. Effects of $[Ca^{2+}]_i$, SR $Ca^{2+}$ load, and rest on $Ca^{2+}$ spark frequency in ventricular myocytes. *Am. J. Physiol* 272:H657–H668.

Schneider, M. F. 1994. Control of calcium release in functioning skeletal muscle fibers. *Annu. Rev. Physiol.* 56:463–484.

Shacklock, P. S., W. G. Wier, and C. W. Balke. 1995. Local $Ca^{2+}$ transients ($Ca^{2+}$-sparks) originate at transverse tubules in rat heart cells. *J. Physiol. (Lond).* 487:601–608.

Shirokova, N., and E. Ríos. 1997. Small event $Ca^{2+}$ release: a probable precursor of $Ca^{2+}$ sparks in frog skeletal muscle. *J. Physiol. (Lond).* 502:3–11.

Smith, G. D., J. E. Keizer, M. D. Stern, W. J. Lederer, and H. Cheng. 1998. A simple numerical model of calcium spark formation and detection in cardiac myocytes. *Biophys. J.* In press.

Song, L.-S., M. D. Stern, E. G. Lakatta, and H. Cheng. 1997. Partial depletion of sarcoplasmic reticulum calcium does not prevent calcium sparks in rat ventricular myocytes. *J. Physiol. (Lond).* 505:665–675.

Spurgeon, H. A., M. D. Stern, G. Baartz, S. Raffaeli, R. G. Hansford, A. Talo, E. G. Lakatta, and M. C. Capogrossi. 1990. Simultaneous measurement of $Ca^{2+}$, contraction, and potential in cardiac myocytes. *Am. J. Physiol.* 258:H574–586.

Stern, M. D., G. Pizarro, and E. Ríos. 1997. Local control model of excitation-contraction coupling in skeletal muscle. *J. Gen. Physiol.* 110:415–440.

Tanaka, H., K. Nishimaru, T. Sekine, T. Kawanishi, R. Nakamura, K. Yamagaki, and K. Shigenobu. 1997. Two-dimensional millisecond analysis of intracellular $Ca^{2+}$ sparks in cardiac myocytes by rapid scanning confocal microscopy: increase in amplitude by isoproterenol. *Biochem. Biophys. Res. Commun.* 233:413–418.

Tsugorka, A., E. Ríos, and L. A. Blatter. 1995. Imaging elementary events of calcium release in skeletal muscle cells. *Science.* 269:1723–1726.

Xiao, R. P., H. H. Valdivia, K. Bogdanov, C. Valdivia, E. G. Lakatta, and H. Cheng. 1997. The immunophilin FK506-binding protein modulates $Ca^{2+}$ release channel closure in rat heart. *J. Physiol. (Lond).* 500: 343–354.